CHEMISTRY OF MATERIALS

pubs.acs.org/cm

Article

Electron-Doped Semiconducting Rocksalt $Al_xSc_{1-x}N$: An Emerging Transparent Conducting Nitride

Subhajit Manna, Sourav Rudra, Prasanna Das, Dheemahi Rao, Rahul Singh Rawat, Aritra Dey, Ashalatha Indiradevi Kamalasanan Pillai, Magnus Garbrecht, and Bivas Saha*

Cite This: https://doi.org/10.1021/acs.chemmater.5c02382

Read Online

ACCESS | Metrics & More | Article Recommendations | Supporting Information

ABSTRACT: Transparent conductors are a unique class of materials that simultaneously exhibit optical transparency and high electrical conductivity, a rare combination critical for many optoelectronic applications. Traditionally, most transparent conductors are oxides or two-dimensional materials, where a wide band gap ensures transparency, while doping-induced free carrier concentrations lead to electrical transport. Here, we present an emerging class of transparent conductors based on III-nitrides, exemplified by electron-doped rocksalt aluminum scandium nitride (r-$Al_{0.56}Sc_{0.44}N$), which exhibits very high optical transparency of ∼98.8% at 550 nm and room temperature electrical conductivity of 19.1 $S.cm^{-1}$. Molecular beam epitaxy deposited, single-crystalline r-$Al_{0.56}Sc_{0.44}N$ exhibits a direct optical band gap of 3.3 eV, facilitating high visible-range solar transparency of ∼85.5% and a small visible spectrum haze ratio of ∼11.6%. Further, high electron concentration arising from oxygen-doping makes r-$Al_{0.56}Sc_{0.44}N$ moderately conductive. Our work establishes electron-doped r-$Al_{0.56}Sc_{0.44}N$ as a promising transparent conducting nitride for solar cells, light-emitting-diodes, liquid-crystal-displays, touchscreens, transparent-heaters, UV-photodetectors, and power electronics applications.

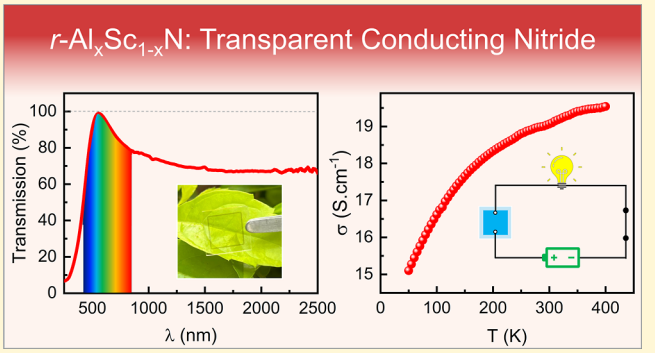

1. INTRODUCTION

Transparent conductors (TCs) are essential materials that combine optical transparency with electrical conductivity, enabling various applications in modern technologies.[1−3] TCs play a crucial role in applications such as touchscreens (see Figure 1a),[1,4] liquid-crystal-displays (LCDs),[5,6] organic light-emitting diodes (OLEDs),[7] smart windows,[8] solar cells,[5,9] flexible electronics,[10,11] transparent-heaters,[12,13] and UV-photodetectors.[14] The performance of a TC is typically determined by its sheet resistance and optical transmittance, with an optimal balance necessary for specific applications. For example, in solar cells, TCs collect charge carriers as electrodes,[5,15] while the front TC film serves as an antireflection coating.[16] Similarly, in light-emitting diodes (LEDs),[17] liquid-crystal and transparent displays,[1,10] TCs act as electrodes and touch sensors in resistive or capacitive touch panels.[10,11] In transparent-heaters or defogging systems, under applied voltage, the heater exhibits a steady rise in temperature, with the heating rate and power consumption closely governed by its sheet resistance.[12,13] However, for widespread industrial applications, along with the high transparency and conductivity, TCs must also exhibit low light absorption,[3] low refractive index,[17] toughness,[11] lower surface energies, thermal and chemical stability.[18,19]

Traditionally, the most well-studied and practically used TCs are oxides, often known as the transparent conducting oxides (TCOs). Among these, indium tin oxide (ITO) is the most commercially used TCO due to its low electrical resistivity and high optical transparency.[5,20] However, alternatives such as aluminum-doped zinc oxide (AZO), gallium-doped zinc oxide (GZO), and fluorine-doped tin oxide (FTO) have gained significant interest due to their lower cost and earth-abundant composition.[7,19,21] While oxygen vacancies have often been proposed as the primary cause of conductivity, defect formation energy calculations with hybrid-functional indicate that these vacancies typically act as deep donors in materials such as ZnO, SnO_2, and β-Ga_2O_3, and therefore cannot fully account for their n-type conductivity.[22−25] Detailed microscopic studies suggest that unintentional hydrogen impurities, either interstitial (H_i) or oxygen-substitutional (H_O), act as shallow donors and are the dominant source of n-type conduction in many oxides.[26] In contrast, the

Received: September 8, 2025
Revised: December 17, 2025
Accepted: December 19, 2025

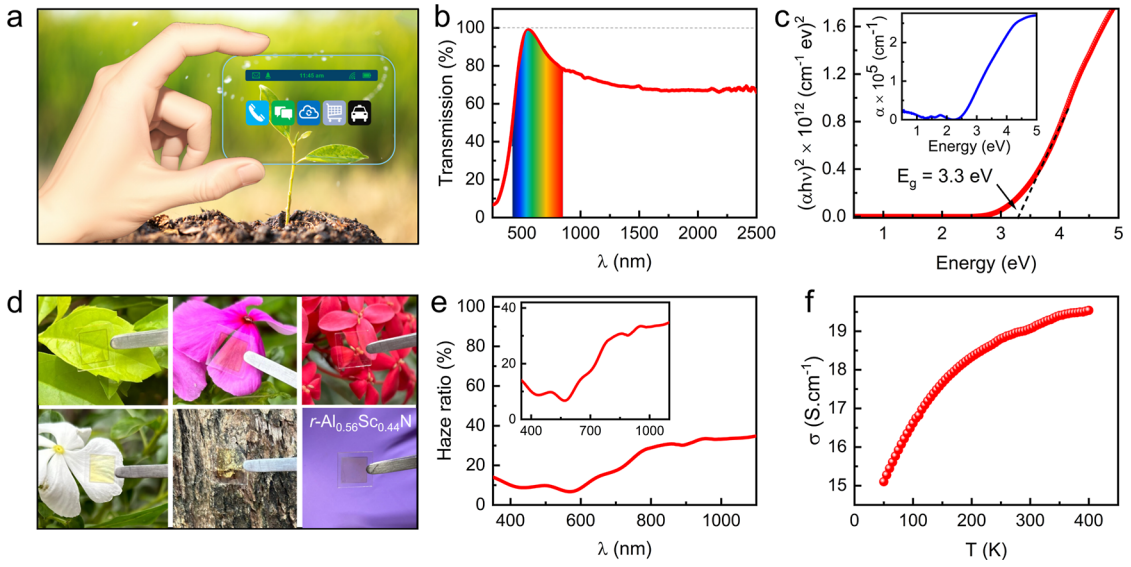

Figure 1. Optical and electrical characterization of r-$Al_{0.56}Sc_{0.44}N$ thin film on (001) MgO substrate. (a) Schematic illustration of a transparent conducting film demonstrating high transparency and suitability for touchscreen applications. (b) The transmission spectrum of r-$Al_{0.56}Sc_{0.44}N$ on a double-sided polished (001) MgO substrate shows excellent transparency in the visible spectral range. (c) The Tauc plot of r-$Al_{0.56}Sc_{0.44}N$ reveals a direct optical band gap of 3.3 eV. (d) Optical images of the r-$Al_{0.56}Sc_{0.44}N$ film under ambient conditions prove its strong transparency in the visible region for practical applications. (e) The haze ratio of the r-$Al_{0.56}Sc_{0.44}N$ shows a low haze value and minimal light scattering. (f) Temperature-dependent electrical conductivity measurement reveals an increase of electrical conductivity with rising temperature, representing an activation-type transport in semiconducting r-$Al_{0.56}Sc_{0.44}N$.

electrical properties of some moderate band gap oxides, such as CdO and $Ba_{1-x}La_xSnO_3$, exhibit intrinsic n-type behavior primarily due to free carriers introduced through extrinsic doping or shallow oxygen vacancies,[27−29] while others display enhanced surface conductivity arising from the lower formation energy of surface oxygen vacancies compared to the bulk, as demonstrated for the (111) surface of In_2O_3.[30] The performance of oxide-based TCs depends on several factors, such as carrier concentration, electron mobility, and film thickness, which influence the trade-off between electrical conductivity and optical transparency. As the demand for efficient and sustainable TCs increases, recent research has focused on optimizing deposition techniques, enhancing mechanical flexibility, and integrating TCOs with complementary metal oxide semiconductor (CMOS) devices for emerging optoelectronic applications.[3,11,31−33]

However, unlike the TCOs, transparent conducting nitrides (TCNs) have remained relatively unexplored for practical applications. The primary reason is the intrinsic electronic structure of nitrides, which generally do not support high free carrier concentrations while maintaining high optical transparency in the visible range.[34] Additionally, depositing stable, good-quality nitride films with high electrical conductivity and visible transparency poses significant challenges due to complex growth conditions and material stability issues. While some studies have investigated the effect of doping on group-III nitrides, such as aluminum-doped gallium nitride, their conductivity and transparency trade-offs remain suboptimal compared to TCOs.[35−39] As a result, TCNs have yet to emerge as viable alternatives to widely used TCOs such as ITO or AZO.[5,7] In this work, we present the first experimental demonstration of plasma-assisted molecular beam epitaxy (PA-MBE) deposited epitaxial and high-temperature-stable ∼100 nm thick r-$Al_{0.56}Sc_{0.44}N$ thin film that simultaneously exhibits moderate electrical conductivity and high optical transparency in the visible spectral range, promising to serve as an alternative to TCOs.

Aluminum scandium nitride ($Al_xSc_{1-x}N$), a solid-state alloy of wurtzite aluminum nitride (AlN) and cubic scandium nitride (ScN), adopts wurtzite or rocksalt crystal structures depending on the Al concentration.[40] At higher Al concentrations, wurtzite-$Al_xSc_{1-x}N$ (w-$Al_xSc_{1-x}N$) has emerged as an excellent piezoelectric and ferroelectric material with large c-axis polarization and is extensively researched for bulk and surface acoustic devices.[41−45] Ferroelectric response in w-$Al_xSc_{1-x}N$ has been utilized recently to develop negative capacitance field effect transistors integrated with 2D MoS_2 monolayers and ferroelectric tunnel junction devices.[46,47] Even at higher Al composition, r-$Al_xSc_{1-x}N$ has been utilized to lattice-match with other metallic transition metal nitrides, such as TiN. Consequently, epitaxial TiN/r-$Al_xSc_{1-x}N$ metal/semiconductor superlattices have been demonstrated to exhibit optical hyperbolic metamaterial properties.[48] Recent theoretical study using the coherent potential approximation shows r-$Al_xSc_{1-x}N$ exhibiting a relatively high X−X direct band gap with moderate Al concentration.[49] Furthermore, experimental research highlights a moderate electron concentration (∼1.1 × 10^{20} cm^{-3}) due to the presence of substitutional oxygen impurities (O_N),[50] making it a potential candidate for TCs. In this work, we present the first conclusive experimental demonstration of r-$Al_xSc_{1-x}N$ as a potential TCN for various device applications.

2. RESULTS AND DISCUSSION

Epitaxial and nominally single-crystalline r-$Al_xSc_{1-x}N$ with x ranging from 0.47 to 0.56 are deposited inside an ultrahigh vacuum PA-MBE, operating at a base pressure of 8.8 × 10^{-11} Torr and substrate temperature of 650 °C (see Section 4.1 in the main text). To ensure the epitaxial nature, (001) MgO substrates exhibiting a rocksalt crystal structure and closely

https://doi.org/10.1021/acs.chemmater.5c02382
Chem. Mater. XXXX, XXX, XXX−XXX

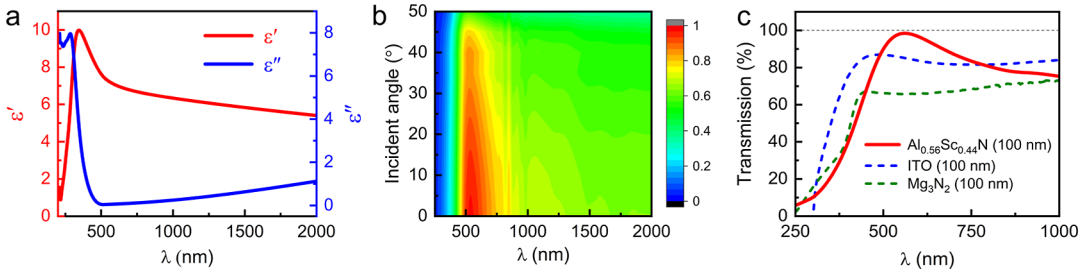

Figure 2. Optical characterization and comparisons of optical properties related to the TC response of *r*-$Al_{0.56}Sc_{0.44}N$. (a) The real (ε') and imaginary (ε'') components of the dielectric permittivity of *r*-$Al_{0.56}Sc_{0.44}N$ on (001) MgO substrate. (b) Angle-dependent transmission spectra of *r*-$Al_{0.56}Sc_{0.44}N$. Transmission is maximum at a zero-degree incident angle, as expected and notably does not reduce much at higher angles of incidence. (c) Comparison of the transmission spectrum of 100 nm *r*-$Al_{0.56}Sc_{0.44}N$ with those of transparent conducting ITO and wide-band gap semiconducting Mg_3N_2, each with a similar thickness of 100 nm.

matched lattice parameters are utilized. The Sc metal source is deliberately exposed to the ambient for oxygen physisorption, so that such oxygen is incorporated inside *r*-$Al_xSc_{1-x}N$ as a dopant during deposition and provides high carrier concentration, causing n-type doping in*r*-$Al_xSc_{1-x}N$ thin films. More details on the structural, optical, and electrical characterization, as well as first-principles density functional theory (DFT) calculations, are presented in the Supporting Information.

Transmission measurements in the near-ultraviolet (UV) to near-infrared (NIR) spectral range exhibit high optical transparency of ∼98.8% at 550 nm (see Figure 1b) in *r*-$Al_{0.56}Sc_{0.44}N$, marking one of the highest transmission values for a TC in the middle of the visible spectrum. The visible-range solar transmittance (T_{solar}) is calculated from the transmission spectrum using eq 1

$$T_{solar} = \frac{\int_{380\ nm}^{720\ nm} T(\lambda) \times I(\lambda)\, d\lambda}{\int_{380\ nm}^{720\ nm} I(\lambda)\, d\lambda} \quad (1)$$

where $T(\lambda)$ represents the film's transmission spectrum and $I(\lambda)$ corresponds to the solar spectral irradiance at the 1.5 AM solar spectrum. The calculated visible-range solar transmittance of 85.5% in *r*-$Al_{0.56}Sc_{0.44}N$ is also very high (see Figure S5 in Supporting Information). A nearly constant transmission of 68 to 70% for the 100 nm film in the near-infrared (NIR) region, covering the tail of the solar spectrum until 2500 nm, as shown in Figure 1b, is observed. The reduction in transmission in the NIR region is attributed to optical losses arising from doping-induced free carrier absorption, as discussed in Supporting Information Section III.[51]

The direct band gap of 3.3 eV, as obtained from the Tauc plot, further confirms the suitability of *r*-$Al_{0.56}Sc_{0.44}N$ for TCNs (see Figure 1c). The absorption coefficient (α) is calculated from the reflection and transmission spectra using eq 2

$$\alpha = \frac{1}{t}\ln\left[\frac{(100 - R)}{T}\right] \quad (2)$$

where t is the thickness of the film, R is the reflection, and T is the transmission. The absorption coefficient (α)-vs-energy plot is shown in the inset of Figure 1c. A sharp decrease in α near ∼2.23 eV (∼557 nm) coincides with high optical transmission. Notably, the slope of $\sqrt{\alpha h\nu}$ as a function of photon energy ($h\nu$) (see Figure S4 in Supporting Information) yields a value of 2.25 eV, highlighting the indirect band gap nature of *r*-$Al_{0.56}Sc_{0.44}N$, where the transmission maximizes, and absorption starts to increase. The experimental absorption onset is lower than its direct band gap, highlighting the phonon-assisted weak optical absorption (see Supporting Information Section III for more details). As shown in the optical images (see Figure 1d), *r*-$Al_{0.56}Sc_{0.44}N$ remains highly transparent in most parts of the visible spectral range, except for the violet region, due to the commencement of band edge absorption. A slight yellowish tone is observed in the film on a white background.

Another key parameter, the haze ratio, quantifies the clarity of transparency in TC materials by determining how much light is scattered during transmission.[52] The 100 nm *r*-$Al_{0.56}Sc_{0.44}N$ thin film exhibits a low haze ratio of ∼11.6% in the visible spectral range, indicating minimal light scattering and high optical transparency (see Figure 1e). A zoomed-in haze ratio plot is shown in the inset of Figure 1e with further details of the haze ratio measurement provided in Section II.5 and Figure S6 in Supporting Information. Further, the temperature-dependent electrical conductivity of *r*-$Al_{0.56}Sc_{0.44}N$ is measured to determine electrical properties. At room temperature, *r*-$Al_{0.56}Sc_{0.44}N$ exhibits an electrical conductivity and carrier concentration of 19.1 $S.cm^{-1}$ and 2.3 × 10^{20} cm^{-3}, respectively. Such a moderate electrical conductivity and carrier concentration in *r*-$Al_{0.56}Sc_{0.44}N$ originate from the intentional oxygen incorporation due to the exposure of Sc source metal to ambient conditions. Since substitutional oxygen at nitrogen sites (O_N) acts as an electron dopant in *r*-$Al_{0.56}Sc_{0.44}N$, it leads to an increase in carrier concentration and, thereby, conductivity. Temperature-dependent (50−400 K) electrical transport measurement shows that the conductivity increases with an increase in temperature (see Figure 1f), with a soft activation nature. The activation energy is calculated as 4.2 meV from the Arrhenius equation (see Figure S10a in Supporting Information), further confirming the semiconducting nature of the film. A video demonstration of conductivity test is included in the Supporting Information.

Further, optical properties, including the dielectric permittivity and angle-dependent transmission spectrum of *r*-$Al_{0.56}Sc_{0.44}N$, are measured using a variable-angle spectroscopic ellipsometer. The imaginary part of dielectric permittivity (ε''), representing optical loss, is low in the longer wavelength regime, while it starts increasing around 375 nm (3.3 eV), representing the direct band gap of *r*-$Al_{0.56}Sc_{0.44}N$ (see Figure 2a). ε'' shows a peak at 285 nm, corresponding to the absorption maximum due to the interband transition from the valence band to a higher unoccupied conduction band at the Γ-point, as shown from the DFT calculations (see Section III

https://doi.org/10.1021/acs.chemmater.5c02382
Chem. Mater. XXXX, XXX, XXX−XXX

Table 1. Electrical Parameters of Oxygen (Electron)-Doped *r*-$Al_{0.56}Sc_{0.44}N$ and Undoped *r*-$Al_{0.5}Sc_{0.5}N$ Films

r-$Al_xSc_{1-x}N$	carrier concentration (cm^{-3})	conductivity ($S.cm^{-1}$)	sheet resistance ($\Omega/\square$)	TC figure-of-merit ($\times 10^{-4}$)
oxygen-doped *r*-$Al_{0.56}Sc_{0.44}N$	2.3×10^{20}	19.1	5.2×10^{3}	1.70
undoped *r*-$Al_{0.5}Sc_{0.5}N$	2.8×10^{19}	5.1	2.5×10^{4}	0.83×10^{-2}

Table 2. Optical and Electrical Parameters of Electron-Doped *r*-$Al_xSc_{1-x}N$ with $x = 0.56$ and $x = 0.47$

% Al	transmission at 550 nm (%)	haze ratio (%)	carrier concentration (cm^{-3})	conductivity ($S.cm^{-1}$)	sheet resistance ($\Omega/\square$)	TC figure-of-merit ($\times 10^{-4}$)
56	98.8	11.6	2.3×10^{20}	19.1	5.2×10^{3}	1.70
47	94.5	7.0	7.6×10^{20}	12.9	7.8×10^{3}	0.70

and Figure S22d of Supporting Information). However, ε'' exhibits a slight increase in the short-wavelength infrared spectral range due to free electron Drude absorptions. The real part of permittivity (ε') decreases slightly in the near-infrared region, whereas it shows a maximum around the band gap energy as the ε' and ε'' are connected through the Kramers–Kronig relationship, consistent with the DFT calculation on oxygen-doped *r*-$Al_{0.5}Sc_{0.5}N$ (see Section III in Supporting Information). The transmission at zero-degree (0°) incident angle reveals a maximum visible transparency at 550 nm (see Figure 2b), consistent with the UV–vis–NIR spectrometer transmission spectrum. Notably, transmission retains its high values at larger angles of incidence, which is necessary for TC applications.

A comparative plot of the optical transmission of 100 nm *r*-$Al_{0.56}Sc_{0.44}N$ with the widely used TCO, such as ITO,[20] as well as wide band gap semiconducting magnesium nitride (Mg_3N_2)[53] with a similar thickness of 100 nm, is shown in Figure 2c. While the 100 nm ITO and Mg_3N_2 thin film exhibits a visible transmission of 85.5% and 65.8% respectively, at 550 nm, the *r*-$Al_{0.56}Sc_{0.44}N$ film shows a higher visible transmission value of 98.8% at the same wavelength. Note, a separate MBE-grown 180 nm Mg_3N_2 film exhibits higher overall transmission than the 100 nm film reported in Figure 2c.[54] Although the transmission at 550 nm for the 100 nm *r*-$Al_{0.56}Sc_{0.44}N$ film is higher than the 180 nm Mg_3N_2, the NIR region transmission is lower due to the free carrier absorption in 100 nm *r*-$Al_{0.56}Sc_{0.44}N$ with a carrier concentration of $\sim 2.3 \times 10^{20}$ cm^{-3}. Overall, these comparisons highlight the potential of *r*-$Al_{0.56}Sc_{0.44}N$ as a high-performance transparent-conducting nitride, especially across the visible range. However, to provide a broad overview of the transmission, sheet resistance, thickness, doping levels, carrier concentration, and related properties of *r*-$Al_xSc_{1-x}N$ and to contextualize these values within the broader transparent-conductor literature, we have compiled all relevant data in Table S1 in Supporting Information.

Furthermore, the Figure-of-Merit (FoM) for a transparent conducting material serves as a key parameter to quantify the trade-off between optical transparency and electrical conductivity.[55] The 100 nm *r*-$Al_{0.56}Sc_{0.44}N$ film shows the FoM of 1.70×10^{-4}, indicating that the oxygen doping enhances its electrical performance compared to undoped *r*-$Al_xSc_{1-x}N$ (see Figure S13 in Supporting Information). While this work marks the first proof-of-concept demonstration, electrical conductivity in *r*-$Al_{0.56}Sc_{0.44}N$ can be improved further by incorporating a higher concentration of oxygen (O_N), leading to a higher electron concentration ($\sim 10^{21}$ cm^{-3}) with improved electrical conductivity.

The carrier concentration of the electron-doped *r*-$Al_{0.56}Sc_{0.44}N$ thin film, as presented in Table 1, is approximately an order of magnitude higher than that of the intentionally undoped *r*-$Al_{0.5}Sc_{0.5}N$ film. This significant increase in free electron density results in a marked enhancement of electrical conductivity in the doped films, underscoring the critical role of intentional doping in tuning the electronic transport properties of *r*-$Al_xSc_{1-x}N$ alloys. Additionally, the transparent conducting Figure-of-Merit (FoM) for the doped film exhibits an improvement of nearly 2 orders of magnitude relative to the undoped counterpart, emphasizing the efficacy of electron doping in optimizing the electrical performance of these materials for transparent conducting applications.

Similarly, a comparative analysis of the optical and electrical properties of oxygen-doped *r*-$Al_xSc_{1-x}N$ thin films with Al concentrations of 56% and 47% is summarized in Table 2. Among the compositions studied, the oxygen (electron)-doped *r*-$Al_{0.56}Sc_{0.44}N$ film exhibits the highest electrical conductivity, lowest sheet resistance, and the highest transparent conducting Figure-of-Merit (*FoM*) (see Figure S13, Supporting Information). These attributes highlight its superior ability to balance optical transparency and electrical conductivity, establishing *r*-$Al_{0.56}Sc_{0.44}N$ as a promising candidate for transparent conducting applications within the oxygen-doped *r*-$Al_xSc_{1-x}N$ material system.

r-$Al_xSc_{1-x}N$ films can also be synthesized using more cost-effective deposition techniques such as magnetron sputtering and other physical vapor deposition methods on a range of substrates, including Al_2O_3, $SrTiO_3$, etc. Indeed, the wurtzite phase of $Al_xSc_{1-x}N$ is already widely employed in industry for piezoelectric sensors, MEMS devices, and ferroelectric functionality-based integrated circuits using sputtering, MBE, and MOCVD-based growth.[41−44] Therefore, while MBE was employed here to demonstrate the transparent conducting properties, other scalable deposition methods are equally feasible for producing *r*-$Al_xSc_{1-x}N$ films.

The structural properties of *r*-$Al_{0.56}Sc_{0.44}N$, analyzed using a high-resolution X-ray diffractometer (HRXRD) (see Figure 3a), show that the thin film grows with a (002) orientation on (001) MgO substrates, forming an epitaxial and nominally single-crystalline layer. The (002) diffraction peak at 41.56° corresponds to an out-of-plane (*c*-axis) lattice constant of 4.34 Å. The rocking curve (ω-scan) corresponding to the (002) diffraction plane exhibits a full-width-at-half-maximum (fwhm) of 0.23° (see Figure 3a, inset), indicating high crystallinity of the film. Furthermore, the Pole figure analysis of the asymmetric (111) plane reveals a 4-fold symmetry, with four equally spaced peaks at an χ angle of 54.7° (see Figure 3b), highlighting the epitaxial nature of the film. The reciprocal space X-ray mapping (RSM) of the asymmetric (113) plane of *r*-$Al_{0.47}Sc_{0.53}N$ is performed to understand the epitaxy and growth details further. As shown in Figure 3c, the centers of the diffraction peaks for the film and substrate are slightly

https://doi.org/10.1021/acs.chemmater.5c02382
Chem. Mater. XXXX, XXX, XXX−XXX

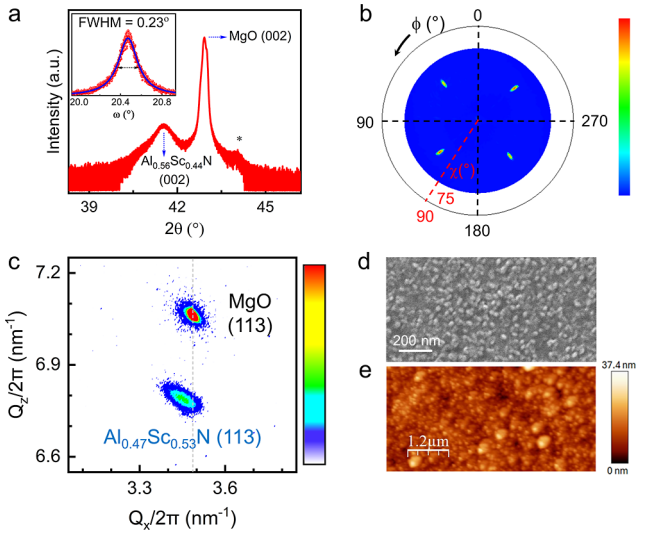

Figure 3. Structural characterization of r-$Al_{0.56}Sc_{0.44}N$ thin film on (001) MgO substrate. (a) Symmetric 2θ-ω X-ray diffraction pattern of (002) oriented r-$Al_{0.56}Sc_{0.44}N$ thin film on (001) MgO substrate. The rocking curve with fwhm is shown in the inset. A small peak around 44.03°, as marked by an asterisk, corresponds to the stage peak of the instrument. (b) The pole figure of the asymmetric (111) plane of r-$Al_{0.56}Sc_{0.44}N$ shows four equally spaced diffraction spots, highlighting the 4-fold symmetric cubic epitaxial nature of the film. (c) The reciprocal space mapping (RSM) of the asymmetric (113) plane of r-$Al_{0.47}Sc_{0.53}N$. (d) Plan-view FESEM image of r-$Al_{0.56}Sc_{0.44}N$ showing the granular-shaped surface morphology. (e) The atomic force microscopy image of r-$Al_{0.56}Sc_{0.44}N$ exhibits a granular-shaped surface with an average root-mean-square roughness of 3.7 nm.

shifted from the vertical line at the same Q_x, as indicated by the dashed line. Such a small shift in Q_x confirms that the film has undergone partial strain relaxation, with its in-plane lattice parameter ($a_{\parallel\text{-film}}$ = 4.25 Å) differing slightly from the substrate ($a_{\parallel\text{-substrate}}$ = 4.21 Å). However, since the spread of the diffraction peak covers the vertical line, a small portion of the film's in-plane lattice parameter aligns with that of MgO and remains pseudomorphic. This mixed behavior indicates that the film undergoes nonuniform strain relaxation. However, the out-of-plane lattice constant ($a_{\perp\text{-film}}$ = 4.37 Å), obtained from the RSM, is slightly higher than the in-plane and MgO lattice constants. This is further corroborated by strain mapping from the high-resolution transmission electron microscopy (HRTEM) data, as discussed in Figure 4d,e. Additionally, the long-term stability and performance of the film have been explored after keeping the film in the ambient for a prolonged time of 16 months without any surface capping layer, as discussed in the Supporting Information Section II.11 and Figure S15.

The field emission scanning electron microscopy (FESEM) plan-view image of r-$Al_{0.56}Sc_{0.44}N$ shows the granular-shaped morphology of the surface, as shown in Figure 3d. The thickness of the film, as determined from cross-sectional FESEM imaging, is ∼100 nm (see Figure S2 in Supporting Information). Furthermore, the atomic force microscopy (AFM) imaging of r-$Al_{0.56}Sc_{0.44}N$ confirms the granular-type morphology with a root-mean-square (RMS) surface roughness of 3.7 nm, as shown in Figure 3e.

The microstructure of r-$Al_{0.47}Sc_{0.53}N$ thin film is analyzed using transmission electron microscopy (TEM), high-angle annular dark field scanning transmission electron microscopy

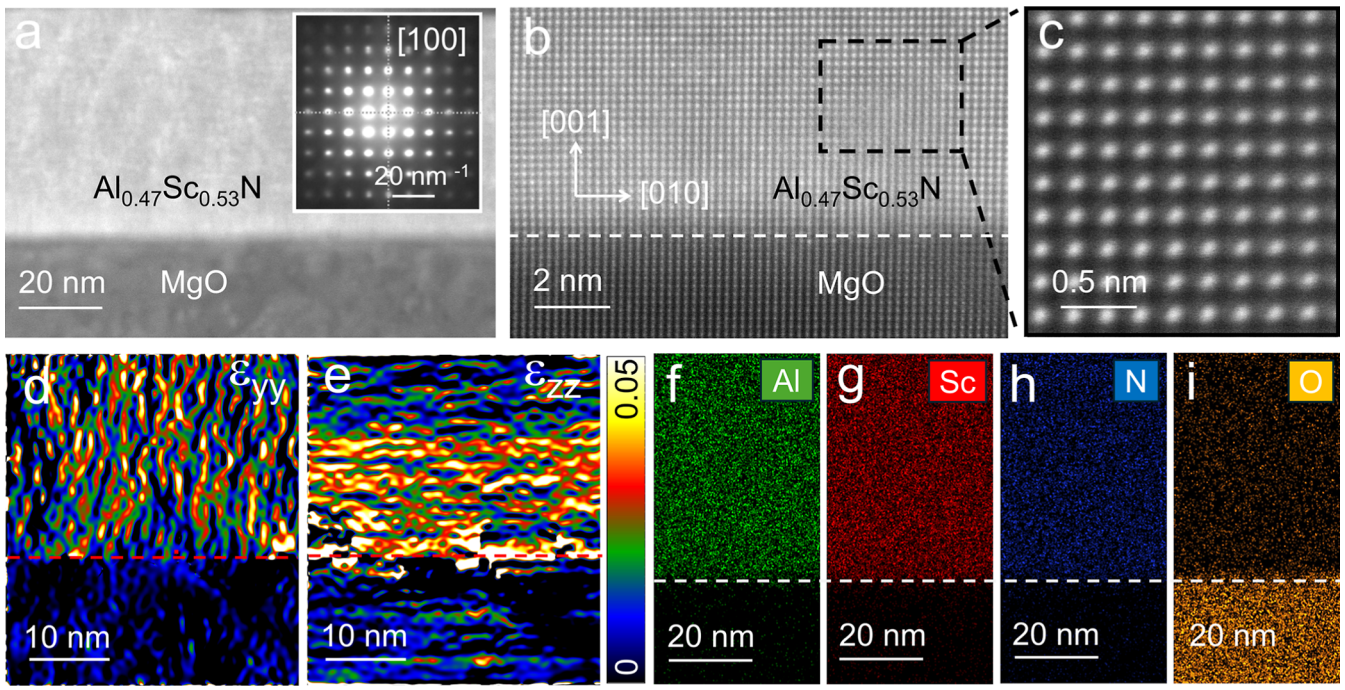

Figure 4. High-resolution transmission electron microscopy imaging of r-$Al_{0.47}Sc_{0.53}N$ on (001) MgO substrate. (a) The TEM image shows a coherent growth of r-$Al_{0.47}Sc_{0.53}N$ on the (001) MgO substrate with a sharp interface. The inset shows the selected area electron diffraction (SAED) pattern along the [100] zone axis of r-$Al_{0.47}Sc_{0.53}N$, confirming the epitaxial growth on MgO. (b) A high-resolution HAADF-STEM image highlights the coherent layer-by-layer growth of r-$Al_{0.47}Sc_{0.53}N$ on MgO substrate. (c) Zoomed-in HAADF-STEM data of r-$Al_{0.47}Sc_{0.53}N$ showing the column of atoms. geometric phase analysis (GPA) strain mapping of r-$Al_{0.47}Sc_{0.53}N$ (d) along the y-axis, ε_{yy} and (e) along the z-axis, ε_{zz} obtained from HAADF-STEM data. EDS elemental mapping of (f) Al, (g) Sc, (h) N, and (i) O shows a uniform distribution of elements inside the film.

https://doi.org/10.1021/acs.chemmater.5c02382
Chem. Mater. XXXX, XXX, XXX−XXX

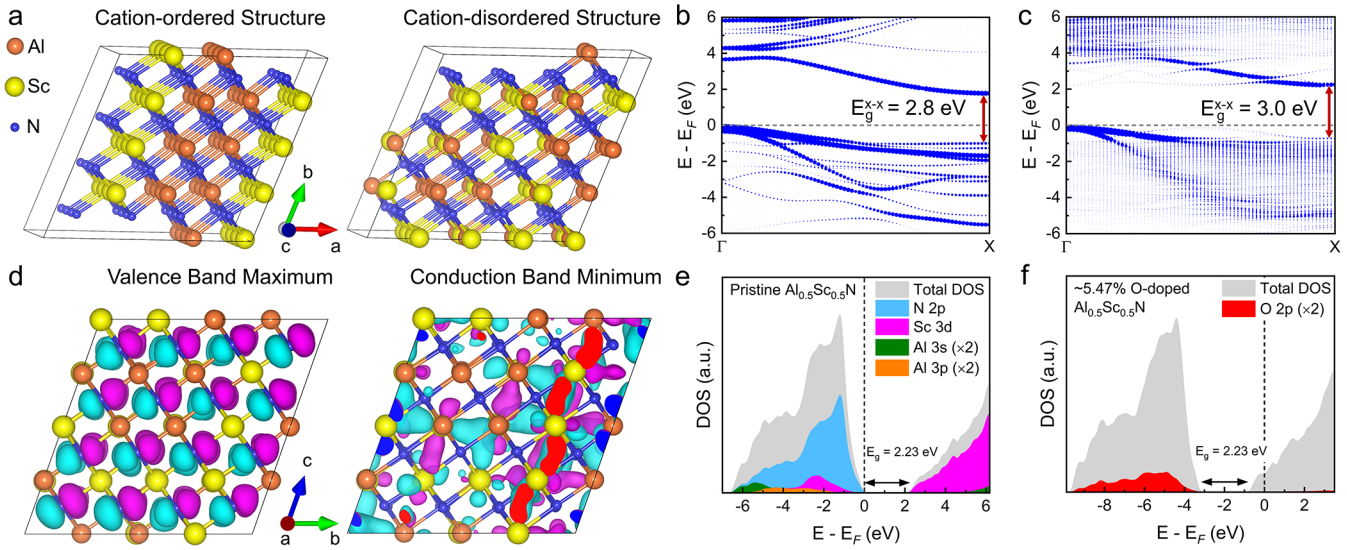

Figure 5. First-principles DFT calculated electronic band structure, real space wave function, and total and projected density of states of *r*-$Al_{0.5}Sc_{0.5}N$. (a) Cation-ordered and cation-disordered 4 × 4 × 4 supercells of the primitive cell structure of *r*-$Al_{0.5}Sc_{0.5}N$, containing 128 atoms. Al, Sc, and N atoms are represented by orange, yellow, and blue colors, respectively. (b) Unfolded effective electronic band structure of cation-ordered *r*-$Al_{0.5}Sc_{0.5}N$ along the Γ-X path of the primitive FCC BZ. (c) Effective band structure of cation-disordered SQS structure of *r*-$Al_{0.5}Sc_{0.5}N$ along the Γ-X path of the primitive FCC Brillouin zone. The size of the dots represents the spectral weight during unfolding and has a value between 0 to 1 for disordered alloy systems. (d) The real space wave function character of the valence band maximum and conduction band minimum at respective Γ and X points in the BZ. (e) Total and orbital projected DOS of pristine *r*-$Al_{0.5}Sc_{0.5}N$. (f) Total and O-2p projected DOS of ∼5.47% oxygen-doped *r*-$Al_{0.5}Sc_{0.5}N$, showing the degenerate semiconducting nature with the Fermi level inside the conduction band.

(HAADF-STEM), energy-dispersive X-ray spectroscopy (EDS) mapping, and selected area electron diffraction (SAED). The TEM image (see Figure 4a) shows a well-defined sharp interface between the *r*-$Al_{0.47}Sc_{0.53}N$ and (001) MgO substrate, indicating high-quality epitaxial growth. The SAED pattern (see the inset of Figure 4a) shows the cubic diffraction pattern of the film. Due to the similarity of the crystal structure and closely matched lattice constants between *r*-$Al_{0.47}Sc_{0.53}N$ and (001) MgO substrate, the film appears homogeneous and uniform without grain boundaries. The high-resolution STEM image (see Figure 4b) further confirms the cubic epitaxial growth with an orientational relationship of [001] (001) *r*-$Al_{0.47}Sc_{0.53}N$ ‖ [001] (001) MgO. Due to the *Z*-contrast in HADDF-STEM, where heavier atoms appear brighter, the *r*-$Al_{0.47}Sc_{0.53}N$ layer appears brighter than the underlying (001) MgO substrate. A zoomed-in HAADF-STEM image of *r*-$Al_{0.47}Sc_{0.53}N$ is presented in Figure 4c, showing the underlying cubic nature of the lattice.

Geometric phase analysis (GPA) strain mapping of ε_{yy} (strain along the in-plane *y*-axis) and ε_{zz} (strain along the out-of-plane *z*-axis) are presented in Figure 4d,e. ε_{yy} hotspots appear as small vertical lines, highlighting in-plane distortion of the unit cells. In contrast, ε_{zz} exhibits maxima at the interface and progressively decreases inside the film. On average, ∼5% ε_{zz} is found at the *r*-$Al_{0.47}Sc_{0.53}N$ and (001) MgO interface. Furthermore, EDS mapping demonstrates the uniform distribution of constituent atoms Al, Sc, and N within *r*-$Al_{0.47}Sc_{0.53}N$ thin film, as shown in Figure 4f–h, respectively. Additionally, EDS mapping (see Figure 4i) confirms the presence of uniformly distributed oxygen atoms in the film, which act as dopants in *r*-$Al_{0.47}Sc_{0.53}N$, introducing excess electrons and making it n-type, thereby enhancing its electrical conductivity. From the HRTEM-EDS analysis, ∼5.4 ± 1.1% atomic percent of oxygen is found inside the film.

To understand the electronic and optical properties of *r*-$Al_xSc_{1-x}N$, first-principles density functional theory (DFT) calculations are performed as implemented in the Vienna ab initio simulation package (VASP).[56] The projected augmented wave pseudopotentials with local density approximation (LDA) exchange–correlation functional of Ceperley and Alder are utilized for all the calculations.[57,58] The LDA underestimation of the band gap is corrected using the recently developed LDA-1/2 method.[59−61] Cation-disordered quasi-random supercells (see Figure 5a) are generated using the special quasirandom structures (SQS) generation algorithm as implemented in the alloy theoretic automated toolkit (ATAT) package.[62] The detailed computational methodology is presented in Section III of Supporting Information. The LDA-optimized lattice constant of *r*-$Al_{0.5}Sc_{0.5}N$, a representative of experimental *r*-$Al_{0.56}Sc_{0.44}N$, is 4.25 Å, consistent with the previous literature report using LDA functional.[49,63] However, the obtained lattice constant is slightly lower than the experimental lattice constant of 4.37 Å due to the overbinding of atoms in the LDA exchange–correlation functional.[40,49]

The self-interaction corrected LDA-1/2 electronic band structure of the 4 × 4 × 4 supercell of *r*-$Al_{0.5}Sc_{0.5}N$ in the supercell Brillouin zone (SCBZ) reveals a direct gap of 2.3 eV at the Γ-point. However, the obtained value is lower than the experimentally observed direct band gap of ∼3.3 eV, suggesting the possibility of an indirect fundamental gap in this system. Therefore, an effective band unfolding method is used to unfold the supercell band structure into the primitive cell Brillouin zone.[64] The 128-atom cation-ordered structure shows an indirect Γ-X band gap of 1.85 eV between Γ-X and a direct gap of 2.8 eV at high-symmetry point X (see Figure 5b). In comparison, the random alloy SQS structure exhibits a fundamental Γ-X indirect band gap of 2.3 eV and a direct X–X gap of 3.0 eV (see Figure 5c), close to the experimental direct

https://doi.org/10.1021/acs.chemmater.5c02382
Chem. Mater. XXXX, XXX, XXX−XXX

gap of 3.3 eV. However, the disordered SQS band structure shows the *k*-dependent smearing of bands due to the breaking of translational symmetry and long-range ordering.[65] The band-like feature with an almost sharp spectral function is preserved near the valence band maxima and conduction band minima at Γ and X high-symmetry points, respectively.

However, a key factor contributing to the high optical transparency is a specific feature of the electronic structure, namely, a sufficiently large energy separation (greater than ∼3.1 eV) between the first occupied conduction-band states and the next higher conduction bands in n-type transparent conductors.[23,24] This wide separation suppresses optical transitions of donor electrons within the conduction band under visible-light excitation, which is crucial for maintaining device transparency and functionality. A similar principle also applies to p-type transparent conductors.[66−68] A detailed analysis confirms that these features are also present in the calculated electronic structure of *r*-$Al_{0.5}Sc_{0.5}N$ (see Figure 5b and Figure 5c). The observed conductivity originates from the donor electrons occupying the X-valley, which is significantly away from the next higher lying conduction band states, satisfying the key criterion for transparent conductors. This large energy separation suppresses optical absorption in the visible spectral range.

The real space wave function analysis suggests the valence band edge of *r*-$Al_{0.5}Sc_{0.5}N$ is dominated mainly by N-2p orbitals. At the same time, the conduction band edge shows Sc-3d character (see Figure 5d) and is also evident from the projected density of states (PDOS) as shown in Figure 5e. The charged-defect formation energy calculation[69] reveals the thermodynamic favorability of the formation of O_N and its role as a shallow donor in *r*-$Al_{0.5}Sc_{0.5}N$ for both N-rich as well as Sc- and Al-rich conditions, as shown in Figure S21a,b in Supporting Information, respectively. The shallow donor nature of oxygen is similar to other nitride semiconductors, such as ScN and GaN.[69,70] This highlights the role of oxygen as an electron dopant in *r*-$Al_{0.5}Sc_{0.5}N$ to achieve moderate electrical conductivity. Furthermore, the electronic density of states calculation reveals that the incorporation of moderate oxygen doping (∼5.47%) in *r*-$Al_{0.5}Sc_{0.5}N$ shifts the Fermi level into the conduction band (see Figure 5f), leading to an n-type electronic transport with moderate electrical conductivity. The oxygen impurities (O_N) have no states inside the band gap of *r*-$Al_{0.5}Sc_{0.5}N$, as shown from the PDOS of the oxygen-doped (O_N) system in Figure 5f. This further suggests that the transmission in the visible range is not significantly affected by the incorporation of oxygen impurity, which eventually donates carriers to the conduction band and improves the electrical conductivity.

3. CONCLUSIONS

In conclusion, we demonstrate electron-doped *r*-$Al_{0.56}Sc_{0.44}N$ as an emerging transparent conducting nitride that could be an alternative to traditional TCOs for specific optoelectronic applications. Molecular beam epitaxy deposited epitaxial and single-crystalline *r*-$Al_{0.56}Sc_{0.44}N$ exhibits ∼98.8% transmission at 550 nm, along with a visible-range solar transmittance of 85.5% and a room-temperature electrical conductivity of 19.1 $S.cm^{-1}$. Additionally, it maintains a low haze ratio of ∼11.6% in the visible spectral range, with minimal light scattering during transmission. Such higher visible range transmission and moderate electrical conductivity lead to a high transparent conducting Figure-of-Merit, indicating *r*-$Al_{0.56}Sc_{0.44}N$ as a promising candidate for transparent conductors. Therefore, our findings represent a significant step in developing nitride-based transparent conductors for CMOS-compatible optoelectronic platforms, including touchscreens, solar cells, LCDs, LEDs/OLEDs, transparent-heaters, UV-photodetectors, and next-generation power electronic devices. Moreover, the demonstration of *r*-$Al_xSc_{1-x}N$ as a transparent conductor represents a significant leap toward broadening the technological scope of $Al_xSc_{1-x}N$, complementing its established potential in piezoelectric and ferroelectric devices.

4. METHODS AND EXPERIMENTAL PROCEDURES

4.1. Thin Film Growth. *r*-$Al_xSc_{1-x}N$ (x = 0.56 and 0.47) thin films are deposited on double-sided polished (001) MgO substrates (1 cm × 1 cm) with a plasma-assisted molecular beam epitaxy (PA-MBE) system within an ultrahigh vacuum (UHV) growth chamber with a base pressure of 8.8×10^{-11} Torr. Before deposition, the MgO substrates are cleaned in acetone and methanol using an ultrasonic bath. The MgO substrates are dried under nitrogen gas and thermally degassed in the PA-MBE preparation chamber at 600 °C for 30 min. During the deposition, the substrate temperature is fixed at 650 °C, and the N_2 (99.99999% purity) flow rate is set at 1.5 sccm. For the growth of *r*-$Al_{0.56}Sc_{0.44}N$, the Al (99.99999% purity) and Sc (99.95% purity) Knudsen-cell (K-cell) temperatures are set to 1150 and 1292 °C, respectively. N_2 plasma is generated using 375 W forward and 15 W reflected RF power. The deposition time is 60 min, and the thickness of the films is 100 nm. For *r*-$Al_{0.47}Sc_{0.53}N$ deposition, the Al K-cell temperature is set to 1135 °C while the Sc K-cell temperature remains fixed at 1292 °C, respectively.

4.2. Measurements & Characterizations. Optical transmission and haze ratio measurements are performed using a PerkinElmer Lambda 500 UV−vis−NIR spectrometer. A double-sided polished (001) MgO substrate is used for the baseline measurement. Room temperature electrical properties are measured using the Ecopia HMS-3000 Hall measurement system with the Van der Pauw method under a magnetic field of 0.58 T. The temperature-dependent electrical measurement (50−400 K) is performed using Quantum Design's VersaLab with the linear contact method. Angle-dependent transmission spectra (0°−50°) and dielectric permittivity are measured using a J.A. Wollam RC2 Ellipsometer. HRXRD measurements are performed using a Rigaku SmartLab X-ray diffractometer (Cu−K_α, λ = 1.54 Å). Pole figure measurement is carried out in Bragg−Brentano (BB) geometry by varying the χ angle from 0° to 75°, and RSM measurements are conducted in 0D continuous mode. The FESEM and AFM imaging are performed using the FEI Inspect F50 FESEM system and Asylum Research MFP-3D Origin system. The HAADF-STEM and EDS mapping are performed using the FEI Themis-Z instrument (Sydney) operated at 300 kV, equipped with a ChemiSTEM EDS detector system for ultrahigh-count rates. TEM sample preparation has been performed in the Tescan Amber X 2 Plasma FIB. The XPS measurements are performed using the Thermo Fisher Scientific K-Alpha system, with an Al−K_α monochromatic X-ray source. Before measurement, the surface oxide layers are removed using a 1 keV Ar^+ ion sputtering gun. Detailed experimental procedures are discussed in the Supporting Information Section I.

4.3. Computational Methodology. The first-principles density functional theory calculations are carried out using the Vienna ab initio simulation package. The projected augmented wave pseudopotential and local density approximation (LDA) exchange−correlation functional of Ceperley and Alder are used for electronic structure calculations. The band gap underestimation is corrected using the LDA-1/2 method. The electronic structure calculations are performed on the cation-disordered quasi-random supercells containing 128 atoms, created using the special quasirandom structures (SQS) generation algorithm as implemented in the alloy theoretic automated toolkit (ATAT) package. The optical property calculations were carried out with a 2 × 2 × 2 supercell containing 16 atoms with a *k*-mesh size of 16 × 16 × 16 using the GW version of pseudopotentials

https://doi.org/10.1021/acs.chemmater.5c02382
Chem. Mater. XXXX, XXX, XXX−XXX

as available in VASP. The formation energy of the substitutional oxygen on nitrogen site (O_N) is calculated as a function of the Fermi level position using the screened Heyd, Scuseria, and Ernzerhof (HSE06) hybrid functional with GGA exchange−correlation and PAW pseudopotentials as implemented in the Vienna Ab initio simulation Package (VASP). The formation energies are calculated using the recently developed Python package PyDefect, integrated with VASP. A 2 × 2 × 2 supercell containing 64 atoms is used for the pristine as well as charged defect calculations. The detailed computational methodology, parameters, and additional discussions are incorporated in the Supporting Information Section III.

■ ASSOCIATED CONTENT

Data Availability Statement

The data that support the findings of this study are available from the corresponding author upon reasonable request.

Supporting Information

The Supporting Information is available free of charge at https://pubs.acs.org/doi/10.1021/acs.chemmater.5c02382.

Experimental methodology, computational details, and further discussion. The Supporting Information also contains visible solar transmittance analysis, haze ratio measurements, Figure-of-Merit analysis, XPS analysis, practical demonstration of conductivity performance, and stability over a prolonged time (PDF)

A video demonstration of the conductivity test (MP4)

■ AUTHOR INFORMATION

Corresponding Author

Bivas Saha − *Chemistry and Physics of Materials Unit, Jawaharlal Nehru Centre for Advanced Scientific Research, Bangalore 560064, India; International Centre for Materials Science and School of Advanced Materials, Jawaharlal Nehru Centre for Advanced Scientific Research, Bangalore 560064, India;* orcid.org/0000-0002-0837-1506; Email: bsaha@jncasr.ac.in

Authors

Subhajit Manna − *Chemistry and Physics of Materials Unit, Jawaharlal Nehru Centre for Advanced Scientific Research, Bangalore 560064, India; International Centre for Materials Science, Jawaharlal Nehru Centre for Advanced Scientific Research, Bangalore 560064, India;* orcid.org/0009-0000-6472-1884

Sourav Rudra − *Chemistry and Physics of Materials Unit, Jawaharlal Nehru Centre for Advanced Scientific Research, Bangalore 560064, India; International Centre for Materials Science, Jawaharlal Nehru Centre for Advanced Scientific Research, Bangalore 560064, India*

Prasanna Das − *Chemistry and Physics of Materials Unit, Jawaharlal Nehru Centre for Advanced Scientific Research, Bangalore 560064, India; International Centre for Materials Science, Jawaharlal Nehru Centre for Advanced Scientific Research, Bangalore 560064, India;* orcid.org/0000-0003-1138-7557

Dheemahi Rao − *Chemistry and Physics of Materials Unit, Jawaharlal Nehru Centre for Advanced Scientific Research, Bangalore 560064, India; International Centre for Materials Science, Jawaharlal Nehru Centre for Advanced Scientific Research, Bangalore 560064, India;* orcid.org/0000-0002-1952-3210

Rahul Singh Rawat − *Chemistry and Physics of Materials Unit, Jawaharlal Nehru Centre for Advanced Scientific Research, Bangalore 560064, India; International Centre for Materials Science, Jawaharlal Nehru Centre for Advanced Scientific Research, Bangalore 560064, India*

Aritra Dey − *Chemistry and Physics of Materials Unit, Jawaharlal Nehru Centre for Advanced Scientific Research, Bangalore 560064, India; International Centre for Materials Science, Jawaharlal Nehru Centre for Advanced Scientific Research, Bangalore 560064, India;* orcid.org/0009-0002-4811-3592

Ashalatha Indiradevi Kamalasanan Pillai − *Sydney Microscopy and Microanalysis, The University of Sydney, Camperdown, New South Wales 2006, Australia*

Magnus Garbrecht − *Sydney Microscopy and Microanalysis, The University of Sydney, Camperdown, New South Wales 2006, Australia;* orcid.org/0000-0002-1852-5580

Complete contact information is available at: https://pubs.acs.org/10.1021/acs.chemmater.5c02382

Author Contributions

S.M., P.D., and B.S. conceived this project. S.M., D.R., and R.S.R. deposited thin films. S.R. and B.S. performed theoretical calculations. P.D. and S.M. performed optical characterization. S.M. performed structural characterization. D.R. performed FESEM imaging. A.D. performed temperature-dependent electrical measurements. A.I.K.P. performed TEM sample preparation, and M.G. performed TEM imaging and EDS mapping. S.M. and M.G. performed GPA strain mapping. All authors discussed and contributed to the preparation of the manuscript.

Notes

The authors declare no competing financial interest.

■ ACKNOWLEDGMENTS

S.M. and B.S. acknowledge the support of the International Centre for Materials Science (ICMS) and Sheikh Saqr Laboratory (SSL) in JNCASR. B.S. acknowledges the Anusandhan National Research Foundation (ANRF) in India for a Core Research Grant No. CRG/2023/007061 for financial support. S.R. and P.D. thank the Council of Scientific & Industrial Research (CSIR) for the fellowship. S.M., D.R., R.S.R., and A.D. thank JNCASR for the fellowship. S.R. and B.S. sincerely acknowledge the support and resources provided by PARAM Yukti Facility under the National Supercomputing Mission (NSM), Government of India at the Jawaharlal Nehru Centre for Advanced Scientific Research (JNCASR), Bangalore. M.G. and A.I.K.P. acknowledge the Sydney Microscopy and Microanalysis facilities at the University of Sydney. S.M. acknowledges Tarak Nath Das and Debmalya Mukhopadhyay's help in performing AFM imaging and optical characterizations. S.M. acknowledges Rahul M and Dr. Bidesh Biswas for the helpful discussion regarding haze ratio measurement and RSM analysis.

■ REFERENCES

(1) Gao, J.; Kempa, K.; Giersig, M.; Akinoglu, E. M.; Han, B.; Li, R. Physics of Transparent Conductors. *Adv. Phys.* **2016**, *65* (6), 553−617.

(2) Putzke, C.; Guo, C.; Plisson, V.; Kroner, M.; Chervy, T.; Simoni, M.; Wevers, P.; Bachmann, M. D.; Cooper, J. R.; Carrington, A.; Kikugawa, N.; Fowlie, J.; Gariglio, S.; Mackenzie, A. P.; Burch, K. S.; Îmamoğlu, A.; Moll, P. J. W. Layered Metals as Polarized Transparent Conductors. *Nat. Commun.* **2023**, *14* (1), 3147.

(3) Hu, C.; Zhou, Z.; Zhang, X.; Guo, K.; Cui, C.; Li, Y.; Gu, Z.; Zhang, W.; Shen, L.; Zhu, J. Far-Infrared Transparent Conductors. *Light:Sci. Appl.* **2023**, *12* (1), 98.
(4) Li, S.; Lee, P. S. Development and Applications of Transparent Conductive Nanocellulose Paper. *Sci. Technol. Adv. Mater.* **2017**, *18* (1), 620−633.
(5) Maniyara, R. A.; Graham, C.; Paulillo, B.; Bi, Y.; Chen, Y.; Herranz, G.; Baker, D. E.; Mazumder, P.; Konstantatos, G.; Pruneri, V. Highly Transparent and Conductive ITO Substrates for near Infrared Applications. *APL Mater.* **2021**, *9* (2), 021121.
(6) Dimitrov, D.; Tsai, C.-L.; Petrov, S.; Marinova, V.; Petrova, D.; Napoleonov, B.; Blagoev, B.; Strijkova, V.; Hsu, K. Y.; Lin, S. H. Atomic Layer-Deposited Al-Doped ZnO Thin Films for Display Applications. *Coatings* **2020**, *10* (6), 539.
(7) Kim, H.; Gilmore, C. M.; Horwitz, J. S.; Piqué, A.; Murata, H.; Kushto, G. P.; Schlaf, R.; Kafafi, Z. H.; Chrisey, D. B. Transparent Conducting Aluminum-Doped Zinc Oxide Thin Films for Organic Light-Emitting Devices. *Appl. Phys. Lett.* **2000**, *76* (3), 259−261.
(8) Zhang, L.; Zhou, Y.; Guo, L.; Zhao, W.; Barnes, A.; Zhang, H.-T.; Eaton, C.; Zheng, Y.; Brahlek, M.; Haneef, H. F.; Podraza, N. J.; Chan, M. H. W.; Gopalan, V.; Rabe, K. M.; Engel-Herbert, R. Correlated Metals as Transparent Conductors. *Nat. Mater.* **2016**, *15* (2), 204−210.
(9) Trapalis, A.; Heffernan, J.; Farrer, I.; Sharman, J.; Kean, A. Structural, Electrical, and Optical Characterization of as Grown and Oxidized Zinc Nitride Thin Films. *J. Appl. Phys.* **2016**, *120* (20), 205102.
(10) Datta, R. S.; Syed, N.; Zavabeti, A.; Jannat, A.; Mohiuddin, M.; Rokunuzzaman, M.; Yue Zhang, B.; Rahman, M. A.; Atkin, P.; Messalea, K. A.; Ghasemian, M. B.; Gaspera, E. D.; Bhattacharyya, S.; Fuhrer, M. S.; Russo, S. P.; McConville, C. F.; Esrafilzadeh, D.; Kalantar-Zadeh, K.; Daeneke, T. Flexible Two-Dimensional Indium Tin Oxide Fabricated Using a Liquid Metal Printing Technique. *Nat. Electron.* **2020**, *3* (1), 51−58.
(11) Li, Q.; Tian, Z.; Zhang, Y.; Wang, Z.; Li, Y.; Ding, W.; Wang, T.; Yun, F. 3D ITO-Nanowire Networks as Transparent Electrode for All-Terrain Substrate. *Sci. Rep.* **2019**, *9* (1), 4983.
(12) Yoon, Y.-H.; Song, J.-W.; Kim, D.; Kim, J.; Park, J.-K.; Oh, S.-K.; Han, C.-S. Transparent Film Heater Using Single-Walled Carbon Nanotubes. *Adv. Mater.* **2007**, *19* (23), 4284−4287.
(13) Jang, H.-S.; Jeon, S. K.; Nahm, S. H. The Manufacture of a Transparent Film Heater by Spinning Multi-Walled Carbon Nanotubes. *Carbon* **2011**, *49* (1), 111−116.
(14) Mondal, S.; Wang, D.; Wang, P.; Wu, Y.; Hu, M.; Xiao, Y.; Mohanty, S.; Ma, T.; Ahmadi, E.; Mi, Z. Reconfigurable Self-Powered Deep UV Photodetectors Based on Ultrawide Bandgap Ferroelectric ScAlN. *APL Mater.* **2022**, *10* (12), 121101.
(15) Ho, I. H.; Chang, C.-W.; Chen, Y.-L.; Chang, W.-Y.; Kuo, T.-J.; Lu, Y.-J.; Gwo, S.; Ahn, H. Ultrathin TiN Epitaxial Films as Transparent Conductive Electrodes. *ACS Appl. Mater. Interfaces* **2022**, *14* (14), 16839−16845.
(16) Sung, Y.; Malay, R. E.; Wen, X.; Bezama, C. N.; Soman, V. V.; Huang, M.-H.; Garner, S. M.; Poliks, M. D.; Klotzkin, D. Anti-Reflective Coating with a Conductive Indium Tin Oxide Layer on Flexible Glass Substrates. *Appl. Opt.* **2018**, *57* (9), 2202.
(17) Haldar, A.; Bera, S.; Jana, S.; Bhattacharya, K.; Chakraborty, R. Development of a Cost Effective Surface-Patterned Transparent Conductive Coating as Top-Contact of Light Emitting Diodes. *J. Appl. Phys.* **2014**, *115* (19), 193108.
(18) Kim, H. J.; Kim, U.; Kim, T. H.; Kim, J.; Kim, H. M.; Jeon, B.-G.; Lee, W.-J.; Mun, H. S.; Hong, K. T.; Yu, J.; Char, K.; Kim, K. H. Physical Properties of Transparent Perovskite Oxides (Ba,La)SnO_3 with High Electrical Mobility at Room Temperature. *Phys. Rev. B* **2012**, *86* (16), 165205.
(19) Wang, J. T.; Shi, X. L.; Liu, W. W.; Zhong, X. H.; Wang, J. N.; Pyrah, L.; Sanderson, K. D.; Ramsey, P. M.; Hirata, M.; Tsuri, K. Influence of Preferred Orientation on the Electrical Conductivity of Fluorine-Doped Tin Oxide Films. *Sci. Rep.* **2014**, *4* (1), 3679.
(20) Farid, N.; Sharif, A.; Vijayaraghavan, R. K.; Wang, M.; Chan, H.; Brunton, A.; McNally, P. J.; Choy, K. L.; O'Connor, G. M. Improvement of Electrical Properties of ITO Thin Films by Melt-Free Ultra-Short Laser Crystallization. *J. Phys. D Appl. Phys.* **2021**, *54* (18), 185103.
(21) Lunca-Popa, P.; Chemin, J.-B.; Adjeroud, N.; Kovacova, V.; Glinsek, S.; Valle, N.; El Hachemi, M.; Girod, S.; Bouton, O.; Maris, J. P. Study of Gallium-Doped Zinc Oxide Thin Films Processed by Atomic Layer Deposition and RF Magnetron Sputtering for Transparent Antenna Applications. *ACS Omega* **2023**, *8* (6), 5475−5485.
(22) Oba, F.; Togo, A.; Tanaka, I.; Paier, J.; Kresse, G. Defect Energetics in ZnO: A Hybrid Hartree-Fock Density Functional Study. *Phys. Rev. B* **2008**, *77* (24), 245202.
(23) Singh, A. K.; Janotti, A.; Scheffler, M.; Van de Walle, C. G. Sources of Electrical Conductivity in SnO_2. *Phys. Rev. Lett.* **2008**, *101* (5), 055502.
(24) Varley, J. B.; Weber, J. R.; Janotti, A.; Van de Walle, C. G. Oxygen Vacancies and Donor Impurities in β-Ga_2O_3. *Appl. Phys. Lett.* **2010**, *97* (14), 6−9.
(25) Lyons, J. L.; Steiauf, D.; Janotti, A.; Van de Walle, C. G. Carbon as a Shallow Donor in Transparent Conducting Oxides. *Phys. Rev. Appl.* **2014**, *2* (6), 064005.
(26) King, P. D. C.; Veal, T. D. Conductivity in Transparent Oxide Semiconductors. *J. Phys.: Condens. Matter* **2011**, *23* (33), 334214.
(27) Burbano, M.; Scanlon, D. O.; Watson, G. W. Sources of Conductivity and Doping Limits in CdO from Hybrid Density Functional Theory. *J. Am. Chem. Soc.* **2011**, *133* (38), 15065−15072.
(28) Dixon, S. C.; Scanlon, D. O.; Carmalt, C. J.; Parkin, I. P. N-Type Doped Transparent Conducting Binary Oxides: An Overview. *J. Mater. Chem. C* **2016**, *4* (29), 6946−6961.
(29) Zhang, J.; Liu, N.; Zhang, W.; Ye, J. Exploring the Influence of Oxygen Vacancy on the Transport Behavior of $Ba_{1-x}La_xSnO_3$ Epitaxial Films at Different Doping Regimes. *J. Appl. Phys.* **2023**, *134* (5), 055701.
(30) Lany, S.; Zakutayev, A.; Mason, T. O.; Wager, J. F.; Poeppelmeier, K. R.; Perkins, J. D.; Berry, J. J.; Ginley, D. S.; Zunger, A. Surface Origin of High Conductivities in Undoped In_2O_3 Thin Films. *Phys. Rev. Lett.* **2012**, *108* (1), 016802.
(31) Ponja, S. D.; Sathasivam, S.; Parkin, I. P.; Carmalt, C. J. Highly Conductive and Transparent Gallium Doped Zinc Oxide Thin Films via Chemical Vapor Deposition. *Sci. Rep.* **2020**, *10* (1), 638.
(32) Parra, J.; Olivares, I.; Frieiro, J. L.; Blazquez, O.; Hernandez, S.; Garrido, B.; Sanchis, P. Transparent Conducting Oxides for Optoelectronics and Biosensing Applications. In *2018 20th International Conference on Transparent Optical Networks (ICTON)*; IEEE, 2018; Vol. *2018*, pp 1−4.
(33) Wang, A. X.; Hsu, W.-C. Perspective on Integrated Photonic Devices Using Transparent Conductive Oxides: Challenges and Opportunities. *Appl. Phys. Lett.* **2024**, *124* (6), 060503.
(34) Baron, E.; Goldhahn, R.; Deppe, M.; As, D. J.; Feneberg, M. Influence of the Free-Electron Concentration on the Optical Properties of Zincblende GaN up to 1×10^{20} cm^{-3}. *Phys. Rev. Mater.* **2019**, *3* (10), 104603.
(35) Muth, J. F.; Lee, J. H.; Shmagin, I. K.; Kolbas, R. M.; Casey, H. C.; Keller, B. P.; Mishra, U. K.; DenBaars, S. P. Absorption Coefficient, Energy Gap, Exciton Binding Energy, and Recombination Lifetime of GaN Obtained from Transmission Measurements. *Appl. Phys. Lett.* **1997**, *71* (18), 2572−2574.
(36) Wang, J.; Li, X.; Chen, L.; Liu, T.; Han, Z.; You, S.; Wang, L.; Li, Z.; Hao, Y.; Zhang, J. Report of GaN HEMTs on 8-in Sapphire. *IEEE Trans. Electron Devices* **2024**, *71* (7), 4429−4432.
(37) Li, E.; Hou, L.; Li, L.; Liu, M.; Xi, M.; Wang, X.; Dai, Y. The Study of Electronic Structures and Optical Properties of Al-Doped GaN. *J. Phys.:Conf. Ser.* **2011**, *276* (1), 012044.
(38) Amano, H.; Baines, Y.; Beam, E.; Borga, M.; Bouchet, T.; Chalker, P. R.; Charles, M.; Chen, K. J.; Chowdhury, N.; Chu, R.; De Santi, C.; De Souza, M. M.; Decoutere, S.; Di Cioccio, L.; Eckardt, B.; Egawa, T.; Fay, P.; Freedsman, J. J.; Guido, L.; Häberlen, O.; Haynes,

https://doi.org/10.1021/acs.chemmater.5c02382
Chem. Mater. XXXX, XXX, XXX−XXX

G.; Heckel, T.; Hemakumara, D.; Houston, P.; Hu, J.; Hua, M.; Huang, Q.; Huang, A.; Jiang, S.; Kawai, H.; Kinzer, D.; Kuball, M.; Kumar, A.; Lee, K. B.; Li, X.; Marcon, D.; März, M.; McCarthy, R.; Meneghesso, G.; Meneghini, M.; Morvan, E.; Nakajima, A.; Narayanan, E. M. S.; Oliver, S.; Palacios, T.; Piedra, D.; Plissonnier, M.; Reddy, R.; Sun, M.; Thayne, I.; Torres, A.; Trivellin, N.; Unni, V.; Uren, M. J.; Van Hove, M.; Wallis, D. J.; Wang, J.; Xie, J.; Yagi, S.; Yang, S.; Youtsey, C.; Yu, R.; Zanoni, E.; Zeltner, S.; Zhang, Y. The 2018 GaN Power Electronics Roadmap. *J. Phys. D Appl. Phys.* **2018**, *51* (16), 163001.

(39) Monemar, B.; Lagerstedt, O. Properties of VPE-Grown GaN Doped with Al and Some Iron-Group Metals. *J. Appl. Phys.* **1979**, *50* (10), 6480−6491.

(40) Saha, B.; Saber, S.; Naik, G. V.; Boltasseva, A.; Stach, E. A.; Kvam, E. P.; Sands, T. D. Development of Epitaxial $Al_xSc_{1-x}N$ for Artificially Structured Metal/Semiconductor Superlattice Metamaterials. *Phys. Status Solidi* **2015**, *252* (2), 251−259.

(41) Akiyama, M.; Kamohara, T.; Kano, K.; Teshigahara, A.; Takeuchi, Y.; Kawahara, N. Enhancement of Piezoelectric Response in Scandium Aluminum Nitride Alloy Thin Films Prepared by Dual Reactive Cosputtering. *Adv. Mater.* **2009**, *21* (5), 593−596.

(42) Tasnádi, F.; Alling, B.; Höglund, C.; Wingqvist, G.; Birch, J.; Hultman, L.; Abrikosov, I. A. Origin of the Anomalous Piezoelectric Response in Wurtzite $Sc_xAl_{1-x}N$ Alloys. *Phys. Rev. Lett.* **2010**, *104* (13), 137601.

(43) Fichtner, S.; Wolff, N.; Lofink, F.; Kienle, L.; Wagner, B. AlScN: A III-V Semiconductor Based Ferroelectric. *J. Appl. Phys.* **2019**, *125* (11), 114103.

(44) Wang, D.; Yang, S.; Liu, J.; Wang, D.; Mi, Z. Perspectives on Nitride Ferroelectric Semiconductors: Challenges and Opportunities. *Appl. Phys. Lett.* **2024**, *124* (15), 150501.

(45) HeOlssonWang, Y. R. H. Y., III; WareMoorePradhan, S. D. C. D. K.; HuMaKennedy, Z. S. W. J.; GlavinDuJariwala, N. R. X. D.; Ma, S.; Pradhan, D. K.; Hu, Z.; Du, X.; Kennedy, W. J.; Glavin, N. R.; Olsson, R. H.; Jariwala, D. $Al_{0.68}Sc_{0.32}N$/SiC-Based Metal-Ferroelectric-Semiconductor Capacitors Operating up to 1000°C. *Nano Lett.* **2025**, *25*, 4767−4773.

(46) Song, S.; Kim, K.-H.; Chakravarthi, S.; Han, Z.; Kim, G.; Ma, K. Y.; Shin, H. S.; Olsson, R. H.; Jariwala, D. Negative Capacitance Field-Effect Transistors Based on Ferroelectric AlScN and 2D MoS_2. *Appl. Phys. Lett.* **2023**, *123* (18), 183501.

(47) Song, S.; Kim, K.-H.; Keneipp, R.; Jung, M.; Trainor, N.; Chen, C.; Zheng, J.; Redwing, J. M.; Kang, J.; Drndić, M.; Olsson III, R. H.; Jariwala, D. High Current and Carrier Densities in 2D MoS_2/AlScN Field-Effect Transistors via Ferroelectric Gating and Ohmic Contacts. *ACS Nano* **2025**, *19* (9), 8985−8996.

(48) Saha, B.; Naik, G. V.; Saber, S.; Akatay, C.; Stach, E. A.; Shalaev, V. M.; Boltasseva, A.; Sands, T. D. TiN/(Al,Sc)N Metal/Dielectric Superlattices and Multilayers as Hyperbolic Metamaterials in the Visible Spectral Range. *Phys. Rev. B* **2014**, *90* (12), 125420.

(49) Waack, J. M.; Kremer, M.; Czerner, M.; Heiliger, C. Structural and Electronic Properties of Cubic Rocksalt $Al_xSc_{1-x}N$ Random Alloys from Ab Initio Calculations. *Phys. Rev. B* **2024**, *109* (7), 075142.

(50) Upadhya, K.; Rao, D.; Biswas, B.; Kumar, R.; Bhatia, V.; Pillai, A. I. K.; Garbrecht, M.; Saha, B. Reducing High Carrier Concentration in Rocksalt-$Al_xSc_{1-x}N$ with Mg Acceptor Doping. *Appl. Phys. Lett.* **2021**, *118* (20), 202107.

(51) Deng, R.; Ozsdolay, B. D.; Zheng, P. Y.; Khare, S. V.; Gall, D. Optical and Transport Measurement and First-Principles Determination of the ScN Band Gap. *Phys. Rev. B* **2015**, *91* (4), 045104.

(52) Li, Y.; Fu, Q.; Yu, S.; Yan, M.; Berglund, L. Optically Transparent Wood from a Nanoporous Cellulosic Template: Combining Functional and Structural Performance. *Biomacromolecules* **2016**, *17* (4), 1358−1364.

(53) Shukla, N.; Rudra, S.; Karanje, R.; Mukhopadhyay, D.; Das, P.; Biswas, B.; Baral, M.; Gupta, M.; Saha, B. Strain-Induced Valence Band Splitting Enabling Above-Bandgap Exciton Luminescence in Epitaxial Mg_3N_2 Thin Films. *Chem. Mater.* **2024**, *36* (11), 5563−5573.

(54) Wu, P.; Tiedje, T. Molecular Beam Epitaxy Growth and Optical Properties of Mg_3N_2 Films. *Appl. Phys. Lett.* **2018**, *113*, 082101.

(55) Haacke, G. New Figure of Merit for Transparent Conductors. *J. Appl. Phys.* **1976**, *47* (9), 4086−4089.

(56) Kresse, G.; Furthmüller, J. Efficient Iterative Schemes for Ab Initio Total-Energy Calculations Using a Plane-Wave Basis Set. *Phys. Rev. B* **1996**, *54* (16), 11169−11186.

(57) Kresse, G.; Joubert, D. From Ultrasoft Pseudopotentials to the Projector Augmented-Wave Method. *Phys. Rev. B* **1999**, *59* (3), 1758−1775.

(58) Ceperley, D. M.; Alder, B. J. Ground State of the Electron Gas by a Stochastic Method. *Phys. Rev. Lett.* **1980**, *45* (7), 566−569.

(59) Ferreira, L. G.; Marques, M.; Teles, L. K. Approximation to Density Functional Theory for the Calculation of Band Gaps of Semiconductors. *Phys. Rev. B* **2008**, *78* (12), 125116.

(60) Cui, H.; Yang, S.; Xue, K.-H.; Huang, J.; Miao, X. On the Self-Consistency of DFT-1/2. *J. Chem. Phys.* **2023**, *158* (9), 094103.

(61) Ai, Z.; Yang, S.; Xue, K.-H.; Yang, W.; Huang, J.; Miao, X. DFT-1/2 for Ionic Insulators: Impact of Self-Energy Potential on Band Gap Correction. *Comput. Mater. Sci.* **2024**, *239* (March), 112978.

(62) van de Walle, A.; Tiwary, P.; de Jong, M.; Olmsted, D. L.; Asta, M.; Dick, A.; Shin, D.; Wang, Y.; Chen, L.-Q.; Liu, Z.-K. Efficient Stochastic Generation of Special Quasirandom Structures. *Calphad* **2013**, *42*, 13−18.

(63) Berkok, H.; Tebboune, A.; Saim, A.; Belbachir, A. H. Structural and Electronic Properties of $Sc_xAl_{1-x}N$: First Principles Study. *Phys. B:Condens. Matter* **2013**, *411*, 1−6.

(64) Popescu, V.; Zunger, A. Effective Band Structure of Random Alloys. *Phys. Rev. Lett.* **2010**, *104* (23), 236403.

(65) Bansil, A. Modern Band Theory of Disordered Alloys: Basic Concepts Including a Discussion of Momentum Densities. *Z. Naturforsch. A.* **1993**, *48* (1−2), 165−179.

(66) Woods-Robinson, R.; Xiong, Y.; Shen, J.-X.; Winner, N.; Horton, M. K.; Asta, M.; Ganose, A. M.; Hautier, G.; Persson, K. A. Designing Transparent Conductors Using Forbidden Optical Transitions. *Matter* **2023**, *6* (9), 3021−3039.

(67) Brunin, G.; Ricci, F.; Ha, V.-A.; Rignanese, G.-M.; Hautier, G. Transparent Conducting Materials Discovery Using High-Throughput Computing. *npj Comput. Mater.* **2019**, *5* (1), 63.

(68) Varley, J. B.; Miglio, A.; Ha, V.-A.; van Setten, M. J.; Rignanese, G.-M.; Hautier, G. High-Throughput Design of Non-Oxide *p*-Type Transparent Conducting Materials: Data Mining, Search Strategy, and Identification of Boron Phosphide. *Chem. Mater.* **2017**, *29* (6), 2568−2573.

(69) Kumagai, Y.; Tsunoda, N.; Oba, F. Point Defects and *p*-Type Doping in ScN from First Principles. *Phys. Rev. Appl.* **2018**, *9* (3), 034019.

(70) Mattila, T.; Nieminen, R. M. Ab Initio Study of Oxygen Point Defects in GaAs, GaN, and AlN. *Phys. Rev. B* **1996**, *54* (23), 16676−16682.

https://doi.org/10.1021/acs.chemmater.5c02382
Chem. Mater. XXXX, XXX, XXX−XXX